Monitoring height and greenness of non-woody floodplain vegetation with UAV time series

Wimala van Iersel *, Menno Straatsma, Elisabeth Addink, Hans Middelkoop

Faculty of Geosciences, Utrecht University, PO-box 80115, 3508 TC Utrecht, The Netherlands

ABSTRACT

Vegetation in river floodplains has important functions for biodiversity, but can also have a negative influence on flood safety. Floodplain vegetation is becoming increasingly heterogeneous in space and time as a result of river restoration projects. To document the spatio-temporal patterns of the floodplain vegetation, the need arises for efficient monitoring techniques. Monitoring is commonly performed by mapping floodplains based on single-epoch remote sensing data, thereby not considering seasonal dynamics of vegetation. The rising availability of unmanned airborne vehicles (UAV) increases monitoring frequency potential. Therefore, we aimed to evaluate the performance of multi-temporal high-spatial-resolution imagery, collected with a UAV, to record the dynamics in floodplain vegetation height and greenness over a growing season. Since the classification accuracy of current airborne surveys remains insufficient for low vegetation types, we focussed on seasonal variation of herbaceous and grassy vegetation with a height up to 3 m. Field reference data on vegetation height were collected six times during one year in 28 field plots within a single floodplain along the Waal River, the main distributary of the Rhine River in the Netherlands. Simultaneously with each field survey, we recorded UAV true-colour and false-colour imagery from which normalized digital surface models (nDSMs) and a consumer-grade camera vegetation index (CGCVI) were calculated. We observed that: (1) the accuracy of a UAV-derived digital terrain model (DTM) varies over the growing season and is most accurate during winter when the vegetation is dormant, (2) vegetation height can be determined from the nDSMs in leaf-on conditions via linear regression (RSME = 0.17–0.33 m), (3) the multitemporal nDSMs yielded meaningful temporal profiles of greenness and vegetation height and (4) herbaceous vegetation shows hysteresis for greenness and vegetation height, but no clear hysteresis was observed for grassland vegetation. These results show the high potential of using UAV-borne sensors for increasing the classification accuracy of low floodplain vegetation within the framework of floodplain monitoring.

© 2018 The Authors. Published by Elsevier B.V. on behalf of International Society for Photogrammetry and Remote Sensing, Inc. (ISPRS). This is an open access article under the CC BY-NC-ND license (http://creativecommons.org/licenses/by-nc-nd/4.0/).

1. Introduction

River floodplains have multiple functions that often conflict spatially, such as water conveyance and water storage during peak discharge, hot-spots for biodiversity, agricultural use and space for recreation (Schindler et al., 2014). Restoration projects of floodplain ecology have resulted in a more natural and heterogeneous floodplain vegetation and have enhanced ecological value and biodiversity of the floodplains (Göthe et al., 2016; Straatsma et al., 2017). The drawback is that developing more natural floodplain vegetation results in increasing hydraulic roughness (Lee et al., 2004), which decreases the conveyance capacity of the floodplain

and increases flood risk (Makaske et al., 2011). Hence, up-to-date maps of floodplain vegetation are of high importance for the spatial planning and management of floodplains, to balance the benefits of more natural vegetation with its risks for flooding.

Due to vegetation development, both ecological and hydraulic characteristics of the floodplain vegetation are expected to change over time (Baptist et al., 2004). To document and evaluate these changes, monitoring of floodplain vegetation is essential. Floodplain vegetation is commonly mapped using remote sensing imagery, such as for the Mississippi River (Dieck et al., 2015), Rhine Delta (Houkes, 2008) and Murray-Darling Basin (Eco Logical Australia, 2015). However, reported land-cover classifications show low accuracies for grassland and herbaceous vegetation, due to the spectral and structural similarity of these vegetation types (Geerling et al., 2007; Straatsma et al., 2008; Knotters and

Brus, 2013). In the field, grassland and herbaceous vegetation can be discriminated by their height. Most grassland species have a maximum height up to 0.5 m. Herbaceous vegetation can reach from 0.5 m up to 2.50 m. Vegetation height is not only relevant to distinguish different vegetation types, but it is also a relevant characteristic determining the vegetation's hydraulic roughness during floodplain inundation (Kouwen and Li, 1980).

The above-ground biomass of most floodplain grassland and herbaceous species dies down in winter. Therefore, their variability in height over time is larger than for woody plants, such as shrubs and trees. The recent increase in availability of unmanned airborne vehicles (UAV) offers the potential to increase monitoring frequency compared to conventional airborne imagery with airplanes, because UAVs are relatively inexpensive and easy to deploy (Dandois and Ellis, 2013). Moreover, the spatial resolution of UAV imagery is in the order of centimetres instead of decimetres (conventional airborne) or meters (satellite), which allows for observation of fine-scale spatial patterns. This is desirable, because grassland and herbaceous vegetation can vary at a scale of decimetres to metres, especially when a floodplain is used for grazing.

In theory, the height of an object may be observed from the UAV imagery with photogrammetry by subtracting the digital terrain model (DTM) from the digital surface model (DSM) of the vegetation, resulting in a normalized DSM (nDSM) (Weidner and Förstner, 1995). The extraction of a DTM from a UAV-derived DSM remains challenging, because of the inability to see the terrain surface through a canopy (Baltsavias, 1999). It also remains unclear how well a UAV-derived DSM can estimate the elevation of a vegetated surface, because vegetation has an irregular surface, especially low vegetation like grassland and herbaceous vegetation.

In addition to vegetation height, photosynthetic activity or greenness can also give information on vegetation type (Cihlar et al., 1996), especially when time series of greenness are used (Müller et al., 2015). The simplest sensors to use on a UAV are consumer-grade digital cameras, which can be adjusted to record near-infrared radiation (Nijland et al., 2014). However, it remains unknown whether such a camera yields meaningful time series for natural grassland and herbaceous vegetation. Time series of combined vegetation height and vegetation greenness are already used for monitoring and classification in forestry (Dandois and Ellis, 2013) and agriculture (Bendig et al., 2015), but it has remained unexplored for low vegetation types like grassland and herbaceous vegetation.

The combination of multitemporal height and spectral data may reveal new possibilities to identify vegetation-type specific seasonal changes, as valuable information for vegetation monitoring at floodplain scale. Therefore, the aims of this study were to (1) evaluate the accuracy of a UAV-derived DTM, (2) evaluate the accuracy of vegetation height derived from UAV imagery nDSMs of low floodplain vegetation over a year, (3) evaluate the performance of multitemporal, high-spatial-resolution UAV imagery for extracting temporal vegetation height and greenness profiles of low vegetation in floodplains and (4) assess how changes in height and greenness during one growing season differ among different vegetation types. To achieve our objectives, a field study was performed in a 1 km^2 floodplain along the lower Rhine in the Netherlands.

2. Study area

We studied the Breemwaard floodplain (Fig. 1A), sized 116 ha, which is located on the southern bank of the river Waal in the Netherlands (Fig. 1C). The floodplain used to have a morphologically dynamic character, which disappeared at the end of the 19th century, due to sand and clay excavation and the construction of groins along the channel bank (Peters et al., 2011). Further clay

and sand mining in the 20th century resulted in large pits, which developed into lakes with marshes and small riparian woods still present today. Clay mining for dike reinforcement was combined with nature development after the 1995 flood, and resulted in a large elongated water body. Its swampy northern bank was overgrown by young willow trees, which were cut in 2012 to reduce vegetation roughness.

Today, approximately 30% of the area is used for hay production and is frequently mowed. Several parts of the floodplain are managed by private owners and are used as grazing fields for ponies, as willow fields, or as reed fields. The remaining part is a nature area that is managed by the state forestry, and is pastured by cows and ponies as part of labour-extensive natural management. Some sections within the nature area are fenced off for cattle, and have developed into riparian woodland. This variability in management resulted in a spatially heterogeneous distribution of vegetation types and structure.

Typical floodplain vegetation along the river Waal includes hayfields, agricultural fields, grassland, herbaceous vegetation, thicket and riparian woodland. This study focused on low vegetation, which was categorised into the classes pioneer, natural grassland, production grassland, high herbaceous, low herbaceous and reed vegetation (Fig. 1B). Pioneer vegetation had a cover of less than 25%. The existing pioneer vegetation was often organized in patches of a few individual plants and did not exceed a maximum height of 0.5 m. The remaining surface was bare substrate. Production grassland had a dense surface cover, comprised a low number of species and was all-year lower than 0.5 m. Height of natural grassland also did not exceed 0.5 m, but it was much higher richer in species than production grassland. Herbaceous vegetation contained most different species and was subdivided in a low class, with height up to 0.7 m and a high class, with height up to 2.5 m. Reed vegetation could grow up to 3 m and comprised a relatively low number of species.

3. Methods

The work flow consisted of three consecutive phases (Fig. 2). First, multitemporal field data collection was carried out, consisting of two simultaneous operations, which are measurements of reference data in the field and acquisition of imagery with a UAV. Second, the UAV imagery was processed into point clouds with colour attributes for each time step. Third, terrain height, vegetation height and vegetation greenness were calculated per plot for the analyses. In the analyses we evaluated (1) the use of DSMs as DTM and the selection of the best performing DSM, (2) an nDSM-derived predictor for vegetation height, (3) temporal profiles of vegetation height and greenness, and (4) the patterns in vegetation height versus greenness over time.

3.1. Multitemporal data collection

3.1.1. Field data acquisition

Twenty-eight field plots (around 15 × 15 m; Fig. 1C) with a different average vegetation height of low vegetation were selected during the first survey in February 2015. Initially 26 plots were selected in February 2015, of which 25 plots had a complete time series of 6 time steps. These were supplemented with a pioneer (nr. 5) and high herbaceous (nr. 28) plot in April 2015 to achieve a broader range of variation in these vegetation types. Plot 27 was excluded after June, because it was excavated during recreation of a natural river bank. Plot 15 was excluded in January, because it was flooded then. Species composition was not a factor determining plot selection, because of the dormant state of the vegetation at that time. Outlines of the plots were measured with
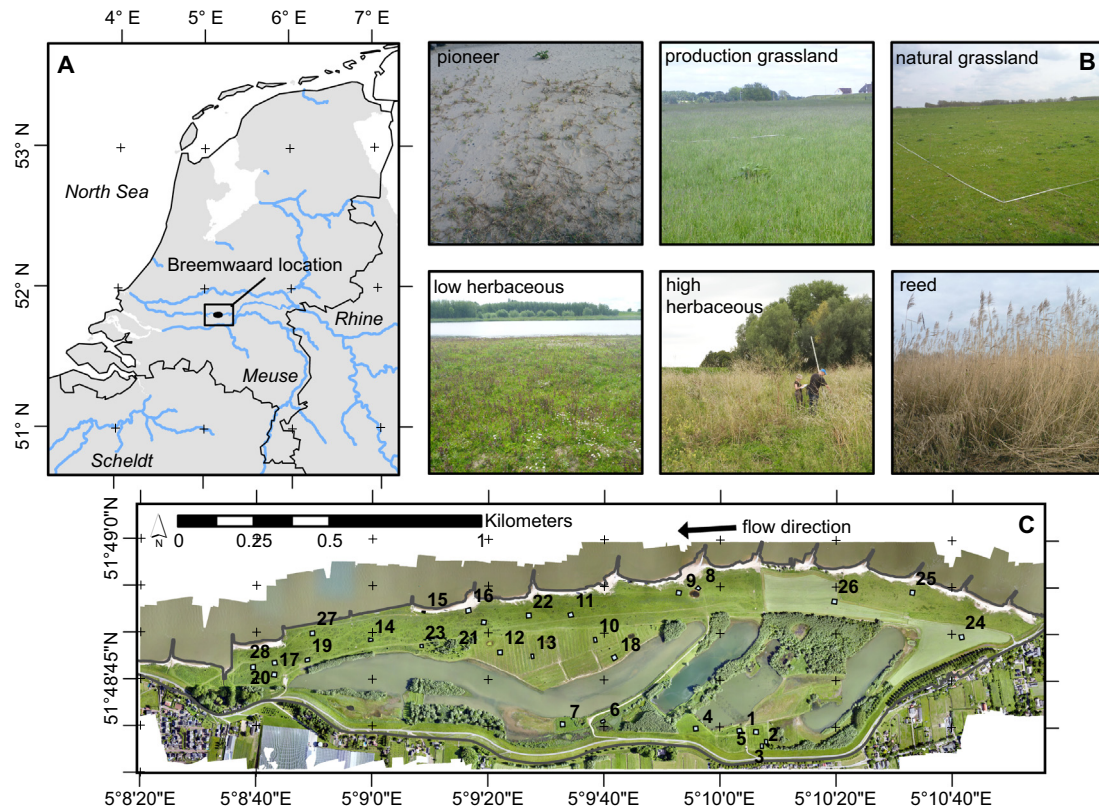
Fig. 1. Location of study area in the Netherlands (A). Field impressions of low floodplain vegetation types (B). Orthophoto of Breemwaard in June 2015 with field plot locations. Black line indicates the boundary of the study area (C).

dGPS. Occasionally, the outline of a plot deviated from the standard 15 × 15 m to maintain homogeneity of the vegetation height in the plot as much as possible.

Vegetation height in the field (VH$_{field}$) was measured six times (February, April, June, September, November 2015 and January 2016) as the mean of 30 individual measurements of randomly selected dominant living plants or the stems of senescent plants. Vegetation height was obtained by placing a measuring rod at random locations in the plot and measuring the maximum height of the closest vegetation element within a 0.1 m radius around the rod. Plots were assigned to a vegetation class based on their maximum average vegetation height over the year and their dominant species composition measured in August.

3.1.2. Image acquisition and georeferencing

During each field survey, the entire study area was recorded with true-colour (RGB) and false-colour (CIR) imagery at 0.05 m resolution with a Canon IXUS 125 HS consumer-grade camera mounted on a UAV (Table 1). For the CIR imagery, a modified Canon IXUS 125 HS was used to enable the recording of near-infrared radiation. The infrared-rejection filter was removed to allow for near infrared (NIR) registration by the camera sensor. The specifications of the replacing filter are classified, but it is expected to be a dual band-pass filter, which transmits only blue, green and near-infrared light (Nijland et al., 2014). In other words, the channels of the RGB camera were red (R), green (G) and blue (B) and of the CIR camera NIR, G and B. Information on channel width of the cameras' sensors is also classified. However, they are expected to be in the range of those reported by Nijland et al. (2014) and LLC LDP (2017), because they used cameras with the same type of sensor (Table 1) to obtain the spectral response curves.

The UAV was mounted with a GPS receiver, altimeter, wind meter and the RGB or CIR camera. The camera was electronically triggered by the autopilot to acquire images at the required positions. All images were georeferenced by the on-board GPS of the UAV. Ground control points (GCPs) for georeferencing of the DSMs were obtained by placing 38 white vinyl markers with a 0.5 m diameter in the field. Five stationary identifiable objects, such as lampposts and road marks on the dike, increased the number of GCPs to 42. The GCPs were distributed over the terrestrial part of the study area and were geolocated with a dGPS, which had an average horizontal and vertical accuracy of 0.015 and 0.02 m respectively. Field reference data of all plots were collected within a two-week period around the UAV flights. Plots with a dense structure were measured after image acquisition to avoid trampled vegetation in the imagery.

3.2. Image and point cloud processing

The UAV images were used to create a coloured point cloud DSM of the study area for each survey using the Structure-from-Motion (SfM) workflow (Lucieer et al., 2014). The SfM processing was carried out in Agisoft PhotoScan Professional version 1.1 (Agisoft, 2014). Important settings in Agisoft are presented in Table 2. The processing workflow in Agisoft consisted of five major steps: (1) excluding poor quality images; (2) building of a sparse point cloud based on image coordinates recorded by the UAV, in order to facilitate identification of GCPs on the images; (3) optimizing the point cloud based on only the GCPs; (4) building of a dense point cloud; and (5) exporting the coloured dense point cloud in LAS format (ASPRS, 2013). The point cloud consisted of the matched points between overlapping images. It represented the digital surface model (DSM) as it includes both terrain and vegeta-
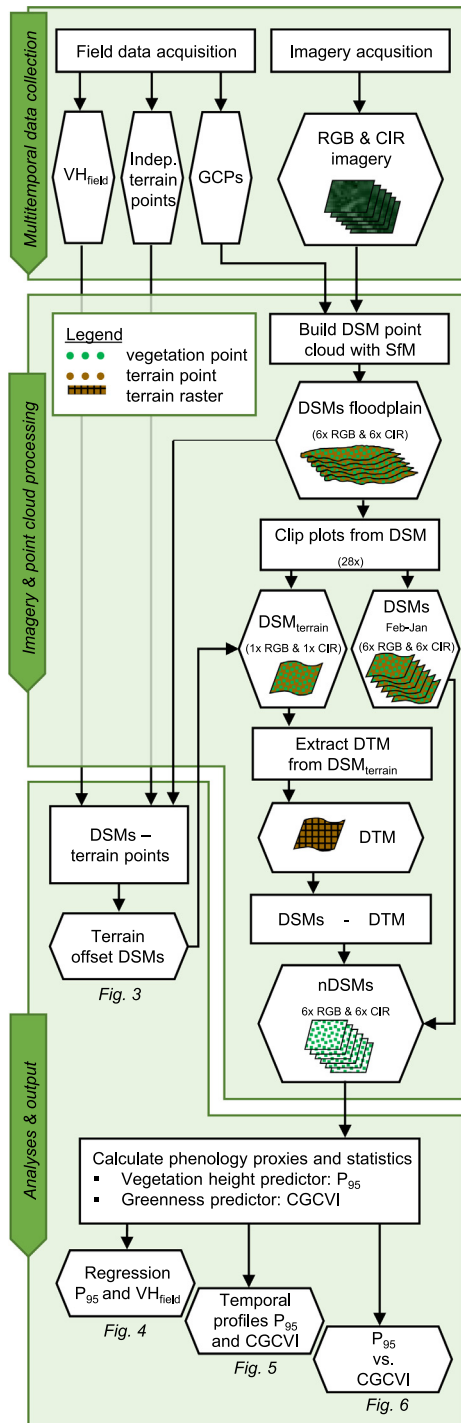
Fig. 2. Processing work flow for RGB and CIR imagery. Six sets of RGB and six sets of CIR imagery were collected in the field and resulted in six RGB and six CIR DSMs of the floodplain via the SfM method. Plot boundaries were clipped from the large DSMs, and resulted in six nDSMs per plot for the analyses.

tion points. The UAV time series resulted in six DSMs of the entire floodplain (Fig. 2), with an average point spacing between 0.08 and 0.11 m. Individual plots were cut from the point clouds using LAStools to limit computation time (LAStools, 2016).

3.3. Analyses

3.3.1. DTMs and nDSMs from UAV imagery
Some points in the plot DSMs represented the terrain, whereas others represented the vegetation. With increasingly higher and

Table 1
Specifications of the UAV, camera and acquired imagery.

UAV and imagery specifications	
UAV	Swinglet CAM by Sensefly
Cameras	Canon IXUS 125 HS
Sensor	resolution16 megapixel CMOS sensor
Ground resolution	5 cm
File format	8-bit JPEG
Acquisition height	150 m
Number of images per survey	275–750
Image overlap	60–80% lat 70–90% lon

Table 2
Settings used for imagery processing in Agisoft.

Agisoft settings	
Excluded images	Quality index <0.5
Key point limit	50,000
Tie point limit	0
Optimized alignment	Markers only (no fit skew & fit k4)
Dense point cloud	High quality, moderate filtering
Exported Points	LAS file

denser vegetation over the growing season fewer points represented the terrain. A digital terrain model (DTM) was necessary for the normalisation of the DSMs, to obtain a model of the vegetation height. However, DTM extraction from UAV imagery is difficult, because the distinction between the vegetation and terrain points is complicated. We derived the DTM from the DSM of the time step which best represented the terrain by identifying the DSM with the smallest terrain offset. We examined how much the RGB and CIR DSMs of each time step deviated from the terrain surface, by comparing them with dGPS reference data. The dGPS measurements at the plot outlines were not used in the DSM creation. To obtain the terrain offset, the dGPS z-coordinates were subtracted from the median z-values of the DSM points in a 0.25 m × 0.25 cm cell at the location of the plot outline dGPS measurements.

For both the RGB and CIR dataset, a DTM was extracted from the DSM with the lowest terrain offset. The selected DSM point cloud was rasterized and the median z-value was assigned to each 0.25 m grid cell, to correct the DTM for noise and the influence of remnant vegetation. As a model for vegetation height, we created a nDSM by subtracting the DTM from the point cloud DSM of each time step.

3.3.2. P_{95} as vegetation height predictor
Vegetation height was predicted using plot level statistics of the nDSMs. We calculated for each plot the 95th percentile (P_{95}) of the z-values of all points from the RGB and CIR based nDSMs, which is a robust statistic given that the number of points exceeded 200,000 points per plot in most cases. We chose P_{95} to represent the dominant vegetation height, similar to the field reference measurements, while excluding outliers (Holman et al., 2016). Moreover, Malambo et al. (2018) conclude that the 90th, 95th and 99th percentile of their SfM point clouds had higher correlations to their crop field height than the maximum, but differences among these statistics were not statistically significant.

An ordinary least squares (OLS) regression between VH_{field} and P_{95} per time step was used to determine how the accuracy of the predicted vegetation height varied over time. An OLS regression is a linear modelling technique to estimate the slope and intercept of the linear function by minimizing the sum of the squares of differences between the observed and predicted values (Montgomery and Peck, 1992). The OLS was executed with the Python Statsmodels package (Perktold et al., 2017). The root mean squared error

(RMSE) of the regression residuals of each time step was used as a measure for the accuracy of P_{95} to predict the reference VH_{field}. This accuracy is important to estimate the signal-to-noise ratio of the vegetation height predictions at the different time steps. Hence, we were able to evaluate the accuracy of the nDSMs obtained from UAV imagery for extracting vegetation height of low floodplain vegetation over one year. The regression functions were not used for further analyses in Sections 3.3.3 and 3.3.4.

3.3.3. Temporal profiles of vegetation height and greenness

Vegetation height and greenness were used as a proxy for the phenology of grassland and herbaceous floodplain vegetation in our study area. We determined vegetation height and greenness development of low floodplain vegetation for each plot. For each time step, the P95 from each plot-nDSM was taken as vegetation height. The colour information associated with the false colour point cloud DSMs was used to derive a consumer-grade camera vegetation index (CGCVI; Eq. (1)). As green leaves absorb solar radiation very strongly in the visible region and are highly reflective in the near-infrared region (Jensen, 2007), the difference or ratio between the two is an indication of the greenness of the vegetation (Tucker, 1979). The CGCVI is similar to the more commonly used Normalized Difference Vegetation Index (NDVI), but is calculated without radiometrically calibrated bands. A normalized ratio shows a stronger correlation with greenness of vegetation compared to a simple ratio of visible and infrared (Tucker, 1979). In this study, for visible radiation blue light is taken instead of the more commonly used red, similar to Rasmussen et al. (2016), because the red sensitivity was replaced by NIR sensitivity in our sensor.

$$CGCVI = \frac{NIR - B}{NIR + B} \tag{1}$$

In Eq. (1) *NIR* is the digital number of near-infrared radiation (0–255) and *B* is the digital number of blue radiation. Per plot, *NIR* and *B* were the averages of the band digital numbers of all points to calculate its average CGCVI. The point clouds were used instead of orthophotos to minimalize data loss due to gridding. CGCVI values were not validated, because they are not based on radiometrically calibrated data.

3.3.4. Vegetation height vs. greenness

To further document and quantify seasonal changes in phenology of the vegetation, we investigated our multitemporal data in a feature space of the predictors for vegetation height and greenness. Per plot the temporal change of vegetation height was compared to its change in greenness by plotting P95 based on the CIR nDSM ($P_{95,CIR}$) against CGCVI over time. Hence, the temporal relation between vegetation height and greenness for the different vegetation types could be investigated at plot level. Moreover, the relationship between vegetation height and greenness was quantified by calculating the area of the resulting hysteresis polygon (see Supplementary Information).

4. Results

4.1. Plot vegetation composition and height

From the vegetation recordings of the field plots in August 2015, we found some overlap in dominant species between the classes (Table 3), but the maximum height they reached over the growing season was very different and most likely determined by the a-biotic conditions of a plot's location and pressures such as grazing intensity. Due to year-round grazing by ponies and cows vegetation height in natural grassland plots is lower than in pioneer and production grassland. In addition to the data in Table 3,

we calculated the standard deviation (SD) of the 30 measurements per plot for each time step. In most cases the SDs were approximately 25% of the plot's average measured height, indicating relatively homogeneous plots, but in some heterogeneous plots the SD was up to 85% of the average height.

4.2. DTMs and nDSMs from UAV imagery

The height differences between the DSMs and dGPS z-values at the plot corners varied between the RGB and CIR DSMs (Fig. 3). Differences in DSMs and dGPS heights may be caused by several factors. Firstly, due to wind, grass leaves and herb elements may wave, giving them a slightly different position on consecutive images, which makes matching elements between images difficult, and may result in different height estimations at those specific points. Furthermore, images were acquired in two consecutive flights, during which wind and lighting/shadowing conditions may have changed, again affecting the dense matching process. Finally, the differences may be caused by the spectral differences of the RGB and CIR imagery, affecting image contrast and matching success between images. To account for this spectral effect both an RGB and CIR DTM were derived from the DSMs.

The height differences at the plot corners also varied significantly over the year (Fig. 3). The highest height differences between DSM and terrain reference occurred in leaf-on conditions (April, June, September, November) of each vegetation type. The lowest terrain offsets were obtained for the senescent conditions in February and January. The median of the boxplots in Fig. 3 were closest to zero in February 2015. Therefore, we chose RGB and CIR DSM_{Feb} to extract respectively the RGB DTM and CIR DTM.

The height differences at the plot corners varied not only over time and between RGB and CIR imagery, but also between vegetation types. For pioneer, natural grassland, production grassland and low herbaceous vegetation the median terrain offset at corner points was less than 0.05 m in February. However, high herbaceous and reed vegetation had a median terrain offset of 0.1 and 0.6 m (RGB) or 0.2 and −0.3 (CIR), most likely due to the remaining senescent vegetation from the preceding year and the effect of wind on this remaining vegetation.

The DTMs were used to calculate the point cloud nDSM for each time step of all plots. The two examples shown in Fig. 4 indicate a nDSM in February ($nDSM_{Feb}$) for the high herbaceous plot and one for a natural grassland plot. The nDSM in June ($nDSM_{Jun}$) shows a larger range in z-values and higher maximum z-values in the high herbaceous plot than in the natural grassland plot. In addition, the number of points in the $nDSM_{Feb}$ is larger than the number of points in the $nDSM_{Jun}$ for both plots, while for the more densely vegetated high herbaceous plot the difference between the number of points of $nDSM_{Feb}$ and $nDSM_{Jun}$ is larger in the high herbaceous plot.

4.3. P_{95} as vegetation height predictor

To investigate how well the nDSM P_{95} value functions as predictor for vegetation height measured in the field, VH_{field} was plotted against P_{95} (Fig. 5). February is not shown, as it was used to create the DTMs. An increase in height range was observed of both VH_{field} and P_{95} from April until November. In January the range decreased again, especially in P_{95}, which can be explained by the decreased ability of the imagery to capture the low-density remnant vegetation.

The OLS regressions show large differences in the accuracy to predict VH_{field} with P_{95} for the five different surveys for both the RGB and CIR nDSMs for each plot (Fig. 5). April still shows VH_{field} within the range 0–30 cm, which is close to the vertical accuracy of 0.1 m of the DSMs (Fig. 3) and therefore prone to errors. The slopes of the regression functions for the leaf-on conditions in June,

Table 3
Summary of field data. n = number of field plots. Statistics are calculated from height measurement over the entire growing season. Dominant species were recorded in August 2015.

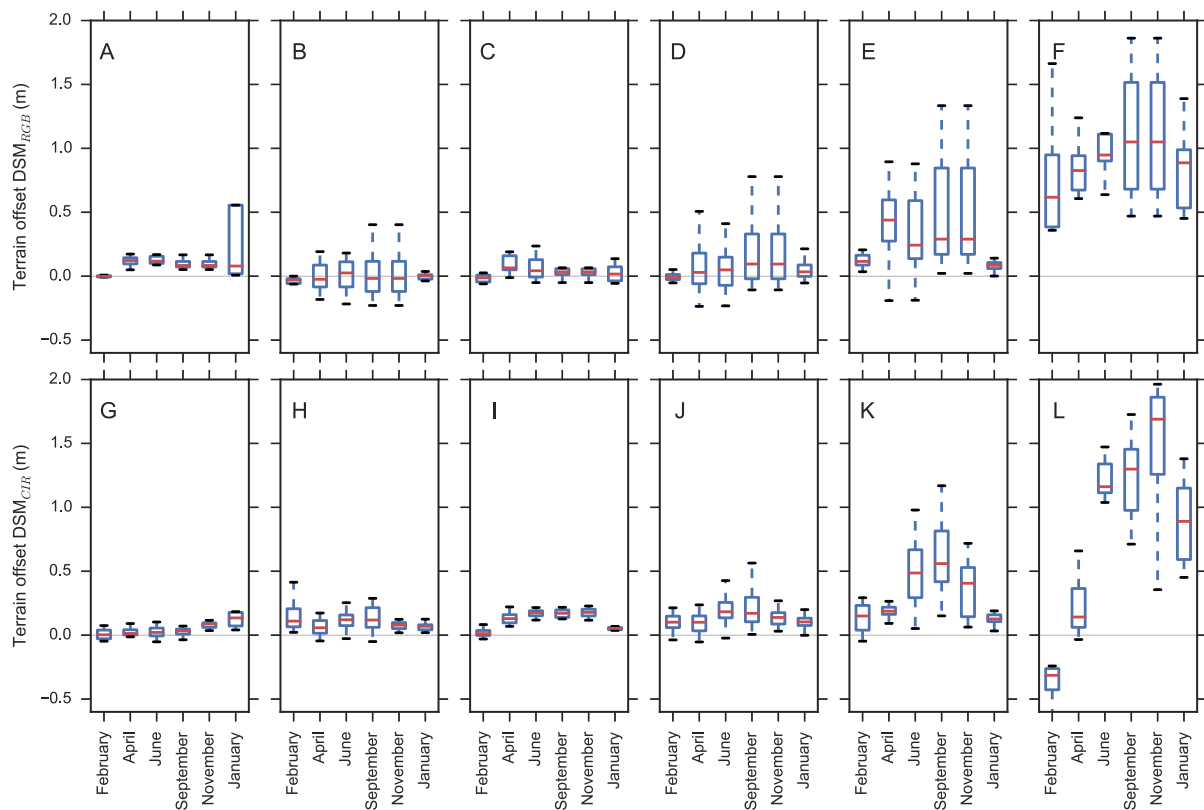| Vegetation type	n	min (m)	max (m)	mean (m)	sd (m)	Dominant species (Latin)	Dominant species (English)
Pioneer	2	0.03	0.44	0.25	0.14	*Cynodon dactylon, Tanacetum vulgare, Lolium perenne, Festuca rubra, Senecio inaequidens*	Scutch grass, Tansy, English ryegrass, Red fescue, Narrow-leaved ragwort
Production grassland	2	0.02	0.67	0.23	0.17	*Lolium perenne, Dactylis glomerata*	English ryegrass, orchard grass
Natural grassland	5	0.03	0.29	0.10	0.08	*Potentilla reptans, Lolium perenne, Trifolium pratense, Achillea millefolium*	Creeping cinquefoil, English ryegrass, Red clover, Yarrow
Low herbaceous	11	0.05	1.12	0.39	0.25	*Plantago lanceolata, Medicago lupulina, Urtica dioica, Rubus caesius, Mentha aquatica, Potentilla reptans*	Narrowleaf plantain, Black medick, Common nettle, Dewberry, Water mint, Creeping cinquefoil
High herbaceous	5	0.11	1.89	1.03	0.47	*Cirsium arvense, Urtica dioica, Brassica nigra*	Creeping thistle, Common nettle, Black mustard
Reed	2	0.21	2.79	1.72	0.88	*Phalaris arundinacea, Convolvulus sepium, Phragmites australis*	Common reed, Reed canary grass, Hedge bindweed

Fig. 3. Vertical accuracy of RGB and CIR DSMs plotted over time per vegetation type: pioneer (A&G, n = 8), natural grassland (B&H, n = 20), production grassland (C&I, n = 8), low herbaceous vegetation (D&J, n = 44), high herbaceous vegetation (E&K, n = 20) and reed (F&L, n = 8). The upper row is based on RGB DSMs and the lower row on CIR DSMs. The box plots show the median with the quartiles as a box around it (P_{25}-P_{75}). The whiskers are showing 1.5 times the interquartile range. In January, one of the pioneer plots flooded during the time of the survey, resulting in a strong overestimation of the elevation with the SfM method.

September and November are close to one. The intercept during these months varies between 0.17 and 0.23 m in the RGB case and between 0.23 and 0.33 m in the CIR case, indicating the magnitude of underestimation of VH_{field} with P_{95}. The R^2 of the RGB regression (0.65–0.87) is higher than the CIR regression (0.55–0.80). The root mean squared error (RMSE) of the OLS regression residuals in the leaf on conditions is 0.17–0.21 m (RGB) and 0.21–0.22 m (CIR). In January, the OLS regression shows inferior results again compared to the leaf-on conditions.

Note that the reed vegetation type was ignored in the regression analyses, due to its relatively large underestimations of P_{95}. Remarkably, this underestimation for reed was not as large in

the CIR nDSMs, as the asterisks representing the reed plots match the extrapolated OLS trend of the other vegetation types (Fig. 5). However, this can be explained by the vertical underestimation of the February CIR DSM (see Fig. 3L), resulting in a misleading correction of the actual underestimation of the reed height.

4.4. Temporal profiles of vegetation height and greenness

Average vegetation height from both the RGB and CIR nDSMs increased until June for pioneer, grassland and low herbaceous vegetation and even until September and November for respectively high herbaceous vegetation and reed (Fig. 6). Subsequently,
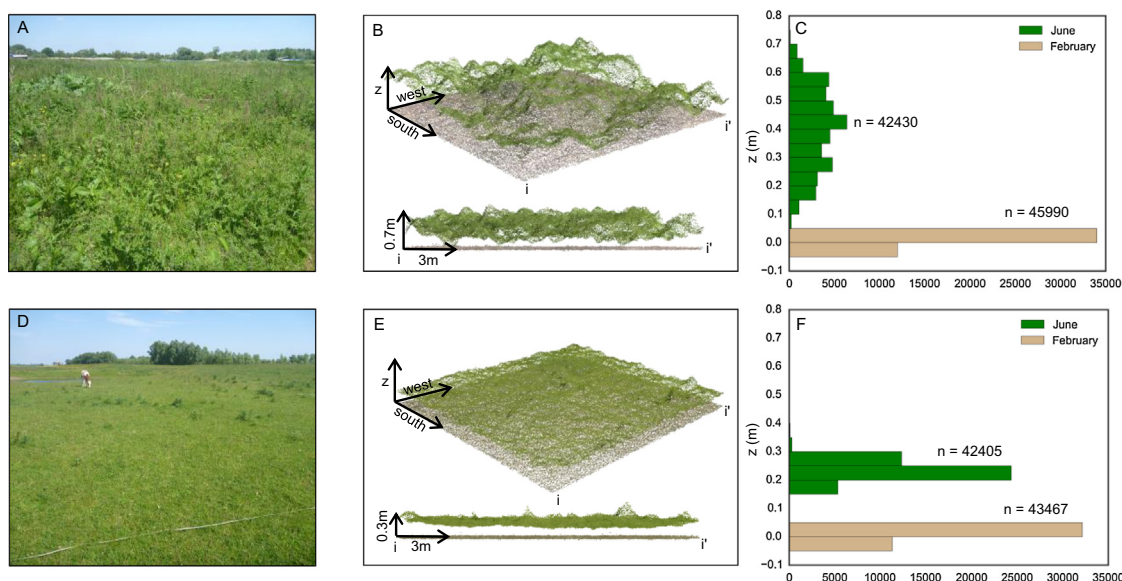
Fig. 4. Examples of true colour nDSM$_{Feb}$ and nDSM$_{Jun}$ point clouds of a high herbaceous plot (B) and a natural grassland plot (E) of 15 × 15 m. Field photographs of June show a larger range in height in the high herbaceous plot (A) compared to the natural grassland plot (D). This is confirmed by the range in z values of the green coloured (RGB) point clouds (B and E). This is even more explicit in the histograms of the z values (C and F). The decrease in point density between February and June is also larger in the high herbaceous vegetation (C) than the natural grassland (F).
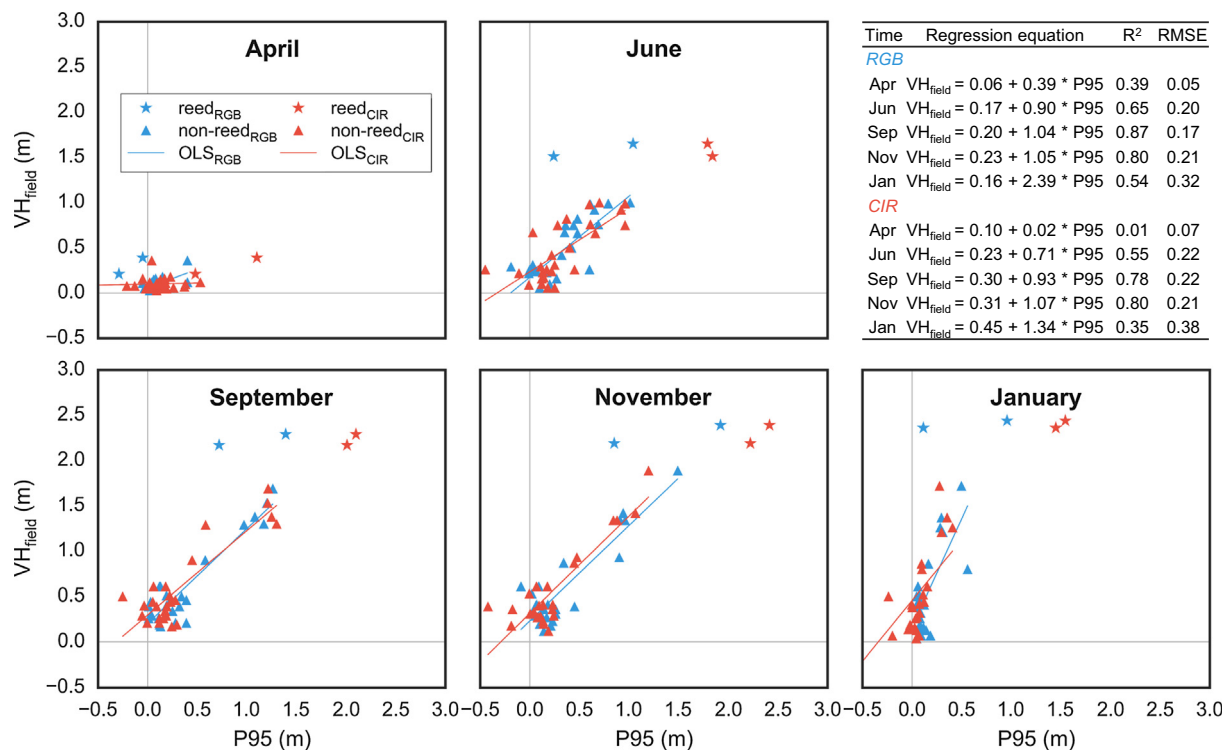

Time	Regression equation	R^2	RMSE
RGB			
Apr	VH$_{field}$ = 0.06 + 0.39 * P95	0.39	0.05
Jun	VH$_{field}$ = 0.17 + 0.90 * P95	0.65	0.20
Sep	VH$_{field}$ = 0.20 + 1.04 * P95	0.87	0.17
Nov	VH$_{field}$ = 0.23 + 1.05 * P95	0.80	0.21
Jan	VH$_{field}$ = 0.16 + 2.39 * P95	0.54	0.32
CIR			
Apr	VH$_{field}$ = 0.10 + 0.02 * P95	0.01	0.07
Jun	VH$_{field}$ = 0.23 + 0.71 * P95	0.55	0.22
Sep	VH$_{field}$ = 0.30 + 0.93 * P95	0.78	0.22
Nov	VH$_{field}$ = 0.31 + 1.07 * P95	0.80	0.21
Jan	VH$_{field}$ = 0.45 + 1.34 * P95	0.35	0.38

Fig. 5. OLS regression between observed vegetation height and predicted vegetation height from the nDSMs. Reed plots (stars) are not included in the regression.

vegetation height decreased again to zero or close to zero. Remnant reed and high herbaceous vegetation probably caused a relatively high vegetation height in January.

The CGCVI showed distinct temporal profiles for each vegetation type. For pioneer vegetation, an increasing trend is observed, even at the end of the growing season. This may be explained by an increasing vegetation cover over time. On average, natural grassland and low herbaceous vegetation show a gradual increase in CGCVI until September, followed by a gradual decrease. Their range between minimum and maximum values is also relatively large compared to the other vegetation types. Production grassland shows a highly variable temporal pattern in CGCVI, because of mowing. High herbaceous vegetation and reed both show an increase in CGCVI until September and a strong decrease until January.

Overall, we observed numerous dissimilarities in the temporal profiles of vegetation height and greenness for the different vegetation types. The next step was therefore to plot the results of the
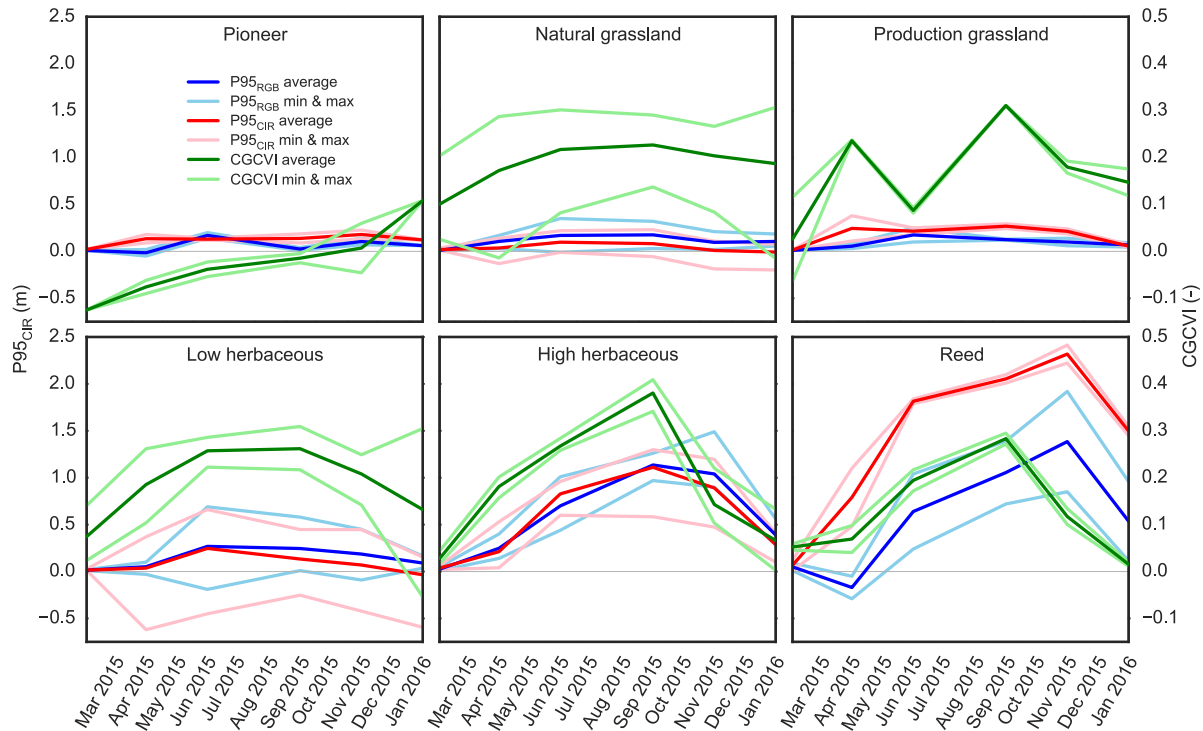
Fig. 6. Timeseries of $P_{95,RGB}$ and $P_{95,CIR}$ and CGCVI from the nDSMs per vegetation type. Light-coloured lines indicate maximum and minimum values. (For interpretation of the references to colour in this figure legend, the reader is referred to the web version of this article.)

different time steps in a feature space of vegetation height and greenness, to study patters of hysteresis between those variables.

4.5. Hysteresis in CGCVI and vegetation height

The hysteresis in the relation between vegetation height, calculated as the $P_{95,CIR}$, and greenness, as CGCVI, over the seasons is strongest for high herbaceous vegetation and reed (Fig. 7). The arrows indicate time and show that plots first become greener followed by an increase in height. Pioneer vegetation does not show hysteresis behaviour. It shows an increase in CGCVI and a minor increase of $P_{95,CIR}$ over time, which is related to increasing vegetation cover over time. For production grassland, the hysteresis shows a complex pattern steered by mowing, which temporarily decreases both CGCVI and $P_{95,CIR}$. In natural grassland and low herbaceous vegetation, CGCVI and $P_{95,CIR}$ show a similar development over the whole year, thus no clear hysteresis. Low herbaceous vegetation plots 10 and 18 (Fig. 7D) showed negative $P_{95,CIR}$ values over their entire growing cycle, which is probably caused by normalization of the DSMs to a locally overestimated DTM. High herbaceous vegetation started with a strong increase in CGCVI and only moderate increase in $P_{95,CIR}$. Later in spring, the P_{95} increased rapidly with a continued increase in CGCVI. In autumn, the CGCVI strongly decreased due to senescence of the herbaceous vegetation, but the high $P_{95,CIR}$ is maintained because of remaining woody dead stems, unlike the less woody grassland and low herbaceous vegetation. These stems are mostly removed during winter by wind or flooding. The hysteresis of reed vegetation is comparable to that of herbaceous vegetation, except for its higher maximum $P_{95,CIR}$ and, therefore, faster $P_{95,CIR}$ increase. Overall, clear differences occurred in the development of CGCVI and $P_{95,CIR}$ over time between the lower pioneer, production grassland, natural grassland, low herbaceous vegetation on the one hand and higher herbaceous and reed vegetation on the other hand. This division is also visible from the resulting polygons, which formed if the first

(February) and last (January) time step per plot in Fig. 7 are connected. We had an insufficient number of plots to calculate polygon area statistics per vegetation type, but the individual polygon areas per plot are in general larger for reed and high herbaceous vegetation than for the lower vegetation types (Supplementary Information).

5. Discussion

Vegetation height and greenness can serve as proxies for phenology of non-woody floodplain vegetation. Accurate vegetation height information is advantageous in the classification of floodplain vegetation, because the class definitions of these types are often based on height thresholds (Edwards, 1983; Verrelst et al., 2009). Moreover, vegetation height is crucial for hydrodynamic roughness estimations (Straatsma et al., 2008), biomass predictions (Bendig et al., 2015) and ecological applications (Davies and Asner, 2014; Vierling et al., 2008). We have shown that low-cost UAV-derived nDSMs can be used to obtain the height of non-woody floodplain vegetation in leaf-on conditions with an accuracy which is acceptable for many applications. Moreover, the hysteresis in the feature space of vegetation height and greenness shows typical patterns for subclasses of non-woody floodplain vegetation. This information is valuable for monitoring of floodplain vegetation, because it can help in discriminating vegetation classes, which are difficult to separate based on single time step data.

5.1. Field data

Our multitemporal field reference data set is unique in the sense that it covers the height of natural vegetation over one year in six time steps. Most studies using remote sensing for height estimation of natural vegetation are validated with single time step datasets (Straatsma and Middelkoop, 2007; Aasen et al., 2015;
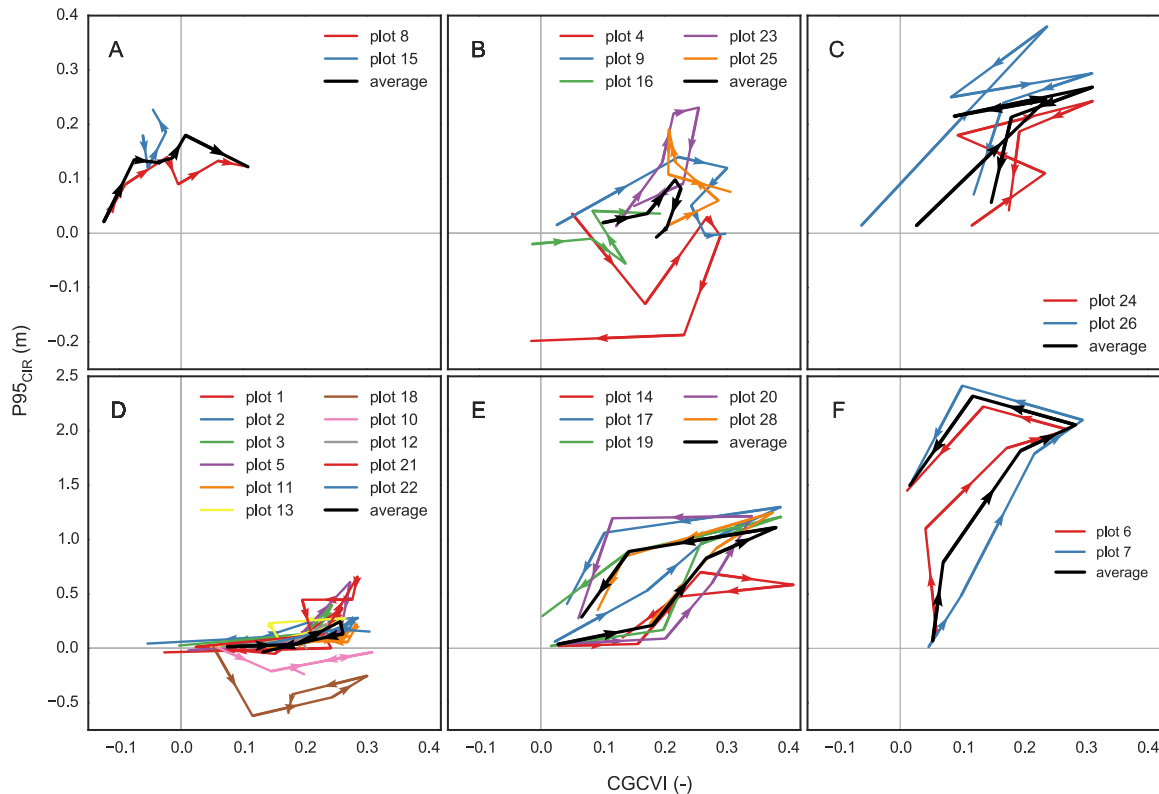
Fig. 7. Hysteresis of CGCVI and $P_{95,CIR}$ over time. Direction of time is indicated by arrows. A. Pioneer, B. Natural grassland, C. Production grassland, D. Low herbaceous vegetation, E. High herbaceous vegetation, F. Reed. Note the different y-axis of A B C and D E F.

Fraser et al., 2016), while our study shows this estimation is time dependent.

Our vegetation height measurements in the field also had a few limitations. The maximum vegetation height is often not derived from the UAV images due to low density of the upper vegetation layer. Conversely, measurements in the field were biased towards higher plants, because we aimed to measure canopy height, by selecting the highest vegetation element within the 0.1 m radius of the measuring rod. Another limitation is the internal heterogeneity of vegetation height in the plots, which is not taken into account, because a plot has its height represented as a single value per time step. The standard deviation of the field measurements offers some insight in the magnitude of the heterogeneity (Table 3). Smaller plots (i.e. 5 × 5 m) with a homogeneous density and canopy height are expected to improve the results of the regression between P_{95} and VH_{field}.

5.2. DTM from UAV imagery

The ability to detect the ground surface using UAV imagery in the study area was best in mid-winter and with senescent vegetation, and decreased over the growing season when the vegetation became higher and denser. Local inaccuracies in the DTM affected the nDSMs, because the DTM was used in the normalization of the DSMs. Compared to the reference terrain measurements, the median terrain offset in February was less than 0.05 m for pioneer, grassland and low herbaceous vegetation, but up to 0.6 m (RGB) and −0.3 (CIR) for reed vegetation (Fig. 3). These results demonstrate that elevation estimates of grass and herbaceous vegetation are highly sensitive to wind effects moving vegetation elements, which increases for tall and flexible vegetation. Using different spectral bands might also influence height accuracy, since at this small spatial scale minor contrast differences can disturb the

matching process in automated DSM generation. Finally, both changing wind and light conditions may result in different elevation estimates when obtained in different flights, even within an hour.

The 0.05 ± 0.05 m vertical accuracy obtained at most plot corners for the DSM_{Feb} is similar to the 7 cm reported vertical accuracy of LiDAR DTMs (Pfeifer et al., 2004; Huising and Gomes Pereira, 1998). However, it is inferior to the 0.006–0.06 m vertical accuracy found by Lucieer et al. (2014), who evaluated the geometric accuracy of an unvegetated landslide DSM using 39 independent dGPS references. Likely explanations are (1) their lower acquisition height of 40 m and higher image overlap (80–90%) compared to 150 m and 60–90% in our study and (2) the bare surface of the landslide, which local variation is much less than for a vegetated surface.

Other studies using UAV imagery to derive vegetation height used different methods to determine the DTM; Bendig et al. (2015) and Possoch et al. (2016) used a DSM of their bare fields before sowing, while Zarco-Tejada et al. (2014) interpolated the ground points between trees. Both methods were no option for the current study, because natural floodplain vegetation does not have a seasonally bare period or sufficient bare ground between objects of interest.

5.3. P_{95} as vegetation height predictor

It is possible for the SfM technique to estimate vegetation height of low floodplain vegetation during leaf-on conditions with an error of approximately 0.20 m or 0.28 m using RGB or CIR imagery respectively. Due to the high vegetation height of herbaceous vegetation, the signal-to-noise ratio remains satisfactory, but the signal of grasslands was lost in the noise in most cases due to its low maximum height. Fraser et al. (2016) found a comparable

standard error of 0.232 m for Arctic shrubs with an imagery resolution of 1.5 cm. For more homogeneous vegetation such as crops, the vertical accuracy is more than a factor 10 higher (Bendig et al., 2014). We found slope and intercept values of our OLS regression comparable to UAV studies monitoring the height of crops (Bendig et al., 2015), trees (Zarco-Tejada et al., 2014), and grass (Possoch et al., 2016).

We recognize three sources of error for the estimated vegetation height from nDSMs. Firstly, the presence of senescent vegetation in February might have caused inaccuracies in the DTM, which affected subsequent normalization of DSMs. The consequence of an error in the DTM is best shown in the reed plots, where an initial underestimation of the DTM caused an overprediction in the subsequent time steps. Local inaccuracies in the February DTM can be caused by the presence of remnant senescent vegetation of the 2014 growing season or local low densities in GCPs. The potential erroneous effect of outliers is unknown. Secondly, the internal variability in plots is represented only by a single value to make the comparison between P_{95} and VH_{field}, which limits the potential of P_{95} and VH_{field} to represent the variety in height *within* the plot. The third source of error explains the observed overall underestimation, which can be more or less than the generally observed 0.2 m, depending on the density of the upper vegetation layer. The underestimation can be expected to be quite low in dense canopies of nettle brushwood, because of their large leaf cover, but may be relatively high in the leafless upper layer of reed vegetation or in dry grassland.

Other UAV-based studies also encountered underestimation of their field vegetation height. Willkomm et al. (2016) suggested that one of the sources of underestimation is movement of plants by wind during image acquisition, preventing the detection of individual leaves emerging from the canopy. This could also be the case for the natural floodplain vegetation, which is exposed to fair amounts of wind due to the openness of the area. Possoch et al. (2016) and Willkomm et al. (2016) state that their errors may be partly explained by their interference with the vegetation while measuring its height. We had a less disturbing method, i.e. without touching the vegetation element to be measured.

Vegetation height predictions based on airborne LIDAR (LIght Detection And Ranging) are a factor 1.5–2 more accurate compared to our UAV-based data (Straatsma and Middelkoop, 2007; Cobby et al., 2001). However, LIDAR is also a much more expensive method, because it is most often collected from a less flexible airborne platform and therefore unattractive to use for multitemporal data collection. Meanwhile, UAV based LIDAR is becoming more widely available (Antero et al., 2016), which leaves the opportunity for future seasonal vegetation monitoring with LiDAR.

5.4. Temporal profiles of vegetation height and greenness

Our multitemporal, high-spatial-resolution UAV imagery performed well for extracting temporal height profiles of low vegetation types in floodplains. A growing phase and senescing phase could be observed in all vegetation types. The temporal P_{95} profiles showed primary differences between vegetation types with a maximum height below 0.5 m and a maximum height between 0.5 and 2.5 m. The duration of the growing phase of the lower vegetation types is months shorter than of the higher vegetation.

Greenness showed more diverse temporal profiles between the vegetation types. Again, reed and high herbaceous vegetation had the longest greening phase. Natural grassland and herbaceous vegetation showed a more balanced greening and withering phase. Typical continued greening and strongly fluctuating profiles were observed for pioneer and production grassland respectively.

The CGCVI was used as a proxy for greenness in this study. An important limitation of the CGCVI is the use of a radiometrically

uncalibrated consumer-grade camera for the calculation of the greenness of the vegetation. Because recording of RAW-format imagery was not possible with the mounted camera, no radiometric information of the images is available after compression into JPEG-format, even if a radiometric calibration would be performed. Moreover, the dual-band-pass filter created NIR sensitivity, but left some sensitivity to red light as well (Nijland et al., 2014). This effect is difficult to quantify without radiometric information. Nonetheless, the CGCVI showed relatively low values in winter and high values in spring and summer. This effect can be attributed to the sensor itself and not to post-processing, because Agisoft simply calculates the average of R, G and B of the overlapping pixels used to calculate a tie point. The camera is thus able to register the normalized change in difference between NIR and B radiation of the vegetation over time, despite the JPEG compression and absence of radiometric calibration of the imagery. Nonetheless, the values were not compared with field spectra and the absolute values and relative changes in CGCVI should be interpreted with care.

Wang et al. (2007) showed a high correlation (0.987) between the common red-based NDVI and a blue-based NDVI based on Landsat imagery. The negligible influence of the atmosphere was in this study the reason to choose blue over red, to calculate the NDVI. The range and values in CGCVI found in this study were lowest for pioneer vegetation, which can be explained by the low vegetation cover in these plots. The largest range (0.0–0.4) was found for high herbaceous vegetation, which can be explained by the relatively higher density of photosynthetic active material (leaves) per m^2 compared to grassland. Lower peak values for reed vegetation may be explained by the presence of remnant reed vegetation in the plots from the year before. Other studies (Fu and Burgher, 2015; Džubáková et al., 2015; Liang et al., 2016) reported NDVI values between 0.25 and 0.72, which generally exceeded our values (Fig. 7), but can be explained by the inclusion of forest plots in their study.

5.5. Hysteresis in CGCVI and vegetation height

The analysis of the relationship between P_{95} and the CGCVI shows different patterns over time for the six vegetation classes. The higher woodiness of high herbaceous and reed vegetation makes them maintain their height during senescence, when photosynthetic activity decreases. This contrasts with grassland and low herbaceous vegetation, which shows a more linear relation between vegetation height and greenness over time. These differences in hysteresis graphs were also expressed in the area of the resulting hysteresis polygon (Supplementary Information). Thus, hysteresis behaviour of these classes can help to differentiate between the low floodplain vegetation types and, therefore, has a high potential to increase classification accuracies.

6. Conclusions

This study presents the first multitemporal analysis of UAV-derived vegetation height and greenness of non-woody floodplain vegetation. From the results of the multitemporal data set collected in this study, we conclude that (1) the accuracy of UAV-derived DTMs varied over a year and was most accurate during winter, (2) vegetation height could be determined from the nDSMs in leaf-on conditions via linear regression (RSME = 0.17–0.33 m), (3) the multitemporal UAV imagery yielded meaningful temporal greenness and height profiles of low vegetation types, (4) greenness and vegetation height showed hysteresis for herbaceous vegetation, but no clear hysteresis for grassland vegetation and (5)

these results show high potential for increasing the classification accuracy of low floodplain vegetation.

Acknowledgements

Appendix A. Supplementary material

Supplementary data associated with this article can be found, in the online version, at https://doi.org/10.1016/j.isprsjprs.2018.04.011.

References

Aasen, H., Burkart, A., Bolten, A., Bareth, G., 2015. Generating 3D hyperspectral information with lightweight UAV snapshot cameras for vegetation monitoring: from camera calibration to quality assurance. ISPRS J. Photogramm. Remote Sens. 108, 245–259.

Agisoft, 2014. PhotoScan Professional 1.1 User Manual. Agisoft, St Petersburg.

Antero, K., Anttoni, J., Hyyppä, J., 2016. The Current State of the Art in UAS-based Laser Scanning. <https://www.gim-international.com/content/article/the-current-state-of-the-art-in-uas-based-laser-scanning> (last accessed March 17, 2017).

ASPRS, 2013. LAS Specification Version 1.4 -R13. <http://www.asprs.org/wp-content/uploads/2010/12/LAS_1_4_r13.pdf> (accessed 22 March, 2017).

Baltsavias, E.P., 1999. A comparison between photogrammetry and laser scanning. ISPRS J. Photogramm. Remote Sens. 54 (2-3), 83–94.

Baptist, M.J., Penning, W.E., Duel, H., Smits, A.J.M., Geerling, G.W., van der Lee, G.E.M., van Alphen, J.S.L., 2004. Assessment of the effects of cyclic floodplain rejuvenation on flood levels and biodiversity along the Rhine river. River Res. Appl. 20 (3), 285–297.

Bendig, J., Bolten, A., Bennertz, S., Broscheit, J., Eichfuss, S., Bareth, G., 2014. Estimating biomass of barley using crop surface models (CSMs) derived from UAV-based RGB imaging. Remote Sens. 6 (11), 10395–10412.

Bendig, J., Yu, K., Aasen, H., Bolten, A., Bennertz, S., Broscheit, J., Gnyp, M.L., Bareth, G., 2015. Combining UAV-based plant height from crop surface models, visible, and near infrared vegetation indices for biomass monitoring in barley. Int. J. Appl. Earth Obs. Geoinf. 39, 79–87.

Cihlar, J., Ly, H., Xiao, Q., 1996. Land cover classification with AVHRR multichannel composites in northern environments. Remote Sens. Environ. 58 (1), 36–51.

Cobby, D.M., Mason, D.C., Davenport, I.J., 2001. Image processing of airborne scanning laser altimetry data for improved river flood modelling. ISPRS J. Photogramm. Remote Sens. 56 (2), 121–138.

Dandois, J.P., Ellis, E.C., 2013. High spatial resolution three-dimensional mapping of vegetation spectral dynamics using computer vision. Remote Sens. Environ. 136, 259–276.

Davies, A.B., Asner, G.P., 2014. Advances in animal ecology from 3D-LiDAR ecosystem mapping. Trends Ecol. Evol. 29 (12), 681–691.

Dieck, J., Ruhser, J., Hoy, E., Robinson, L., 2015. General Classification Handbook for Floodplain Vegetation in Large River Systems (ver. 2.0, November 2015). Tech. Rep. Book 2, U.S. Geological Survey Techniques and Methods.

Džubáková, K., Molnar, P., Schindler, K., Trizna, M., 2015. Monitoring of riparian vegetation response to flood disturbances using terrestrial photography. Hydrol. Earth Syst. Sci. 19 (1), 195–208.

Eco Logical Australia, 2015. Vegetation of the Barwon-Darling and Condamine-Balonne Floodplain Systems of New South Wales Mapping and Survey of Plant Community Types. Tech. rep., Eco Logical Australia.

Edwards, D., 1983. A broad-scale structural classification of vegetation for practical purposes. Bothalia 14 (4), 705–712.

Fraser, R.H., Olthof, I., Lantz, T.C., Schmitt, C., 2016. UAV photogrammetry for mapping vegetation in the low-arctic. Arct. Sci. 102 (June), 1–51.

Fu, B., Burgher, I., 2015. Riparian vegetation NDVI dynamics and its relationship with climate, surface water and groundwater. J. Arid Environ. 113, 59–68.

Geerling, G.W., Labrador-Garcia, M., Clevers, J.G.P.W., Ragas, A.M.J., Smits, A.J.M., 2007. Classification of floodplain vegetation by data fusion of spectral (CASI) and LiDAR data. Int. J. Remote Sens. 28 (19), 4263–4284.

Göthe, E., Timmermann, A., Baattrup-pedersen, A., Januschke, K., 2016. Structural and functional responses of floodplain vegetation to stream ecosystem restoration. Hydrobiologia 769, 79–92.

Holman, F.H., Riche, A.B., Michalski, A., Castle, M., Wooster, M.J., Hawkesford, M.J., 2016. High throughput field phenotyping of wheat plant height and growth rate in field plot trials using UAV based remote sensing. Remote Sens. 8 (12).

Houkes, G., 2008. Toelichting ecotopenkartering Rijntakken-Oost 2005. Tech. rep. Rijkswaterstaat, Data-ICT-Dienst, Delft.

Huising, E.J., Gomes Pereira, L.M., 1998. Errors and accuracy estimates of laser data acquired by various laser scanning systems for topographic applications. ISPRS J. Photogramm. Remote Sens. 53 (5), 245–261.

Jensen, J.R., 2007. Remote Sensing of the Environment: An Earth Resource Perspective. Pearson Prentice Hall.

Knotters, M., Brus, D.J., 2013. Purposive versus random sampling for map validation: a case study on ecotope maps of floodplains in the Netherlands. Ecohydrology 6 (3), 425–434.

Kouwen, N.N., Li, R.-M., 1980. Biomechanics of vegetative channel linings. J. Hydraul. Div. 106 (ASCE 15464).

LAStools, 2016. Efficient LiDAR Processing Software (version 160221, academic) obtained from <http://rapidlasso.com/LAStools>.

Lee, J.K., Roig, L.C., Jenter, H.L., Visser, H.M., 2004. Drag coefficients for modeling flow through emergent vegetation in the Florida Everglades. Ecol. Eng. 22 (4-5), 237–248.

Liang, T., Yang, S., Feng, Q., Liu, B., Zhang, R., Huang, X., Xie, H., 2016. Multi-factor modeling of above-ground biomass in alpine grassland: a case study in the Three-River Headwaters Region, China. Remote Sens. Environ. 186, 164–172.

LLC LDP, 2017. Remote Sensing Cameras. Obtained from <https://www.maxmax.com/maincamerapage/remote-sensing> (accessed 18 December, 2017).

Lucieer, A., de Jong, S.M., Turner, D., 2014. Mapping landslide displacements using Structure from Motion (SfM) and image correlation of multi-temporal UAV photography. Prog. Phys. Geogr. 38 (1), 97–116.

Makaske, B., Maas, G.J., Van Den Brink, C., Wolfert, H.P., 2011. The influence of floodplain vegetation succession on hydraulic roughness: is ecosystem rehabilitation in dutch embanked floodplains compatible with flood safety standards? Ambio 40 (4), 370–376.

Malambo, L., Popescu, S.C., Murray, S.C., Putman, E., Pugh, N.A., Horne, D.W., Richardson, G., Sheridan, R., Rooney, W.L., Avant, R., Vidrine, M., McCutchen, B., Baltensperger, D., Bishop, M., 2018. Multitemporal field-based plant height estimation using 3D point clouds generated from small unmanned aerial systems high-resolution imagery. Int. J. Appl. Earth Obs. Geoinf. 64 (August 2017), 31–42.

Montgomery, D.C., Peck, E.A., 1992. Introduction to Linear Regression Analysis. Wiley.

Müller, H., Rufin, P., Griffiths, P., Barros Siqueira, A.J., Hostert, P., 2015. Mining dense Landsat time series for separating cropland and pasture in a heterogeneous Brazilian savanna landscape. Remote Sens. Environ. 156, 490–499.

Nijland, W., de Jong, R., de Jong, S.M., Wulder, M.A., Bater, C.W., Coops, N.C., 2014. Monitoring plant condition and phenology using infrared sensitive consumer grade digital cameras. Agric. For. Meteorol. 184, 98–106.

Perktold, J., Seabold, S., Taylor, J., 2017. Statsmodels's Documentation Obtained From: <http://www.statsmodels.org/stable/index.html> (accessed 19 December, 2017).

Peters, B., Kurstjens, G., van Diermen, J., 2011. Rijn in beeld Natuurontwikkeling langs de grote rivieren Deel 1 De Waal. Tech. rep., Bureau Drift/Kurstjens Ecologisch Adviesbureau.

Pfeifer, N., Gorte, B., Elberink, O., 2004. Influences of vegetation on laser altimetry analysis and correction approaches. Int. Arch. Photogramm. Sens. Spat. Inf. Sci. XXXVI-8/W2, 283–287.

Possoch, M., Bieker, S., Hoffmeister, D., Bolten, A., Schellberg, J., Bareth, G., Conservation, R., Group, C.S., Conservation, R., Ecology, P., Model, C.S., 2016. Multi-temporal crop surface models combined with the RGB vegetation index from UAV-based images for forage monitoring in grassland. Int. Arch. Photogramm. Remote Sens. Spat. Inf. Sci., 991–998

Rasmussen, J., Ntakos, G., Nielsen, J., Svensgaard, J., Poulsen, R.N., Christensen, S., 2016. Are vegetation indices derived from consumer-grade cameras mounted on UAVs sufficiently reliable for assessing experimental plots? Eur. J. Agron. 74, 75–92.

Schindler, S., Sebesvari, Z., Damm, C., Euller, K., Mauerhofer, V., Schneidergruber, A., Biró, M., Essl, F., Kanka, R., Lauwaars, S.G., Schulz-Zunkel, C., van der Sluis, T., Kropik, M., Gasso, V., Krug, A., Pusch, M.T., Zulka, K.P., Lazowski, W., Hainz-Renetzeder, C., Henle, K., Wrbka, T., 2014. Multifunctionality of floodplain landscapes: relating management options to ecosystem services. Landsc. Ecol. 29 (2), 229–244.

Straatsma, M.W., Baptist, M.J., 2008. Floodplain roughness parameterization using airborne laser scanning and spectral remote sensing. Remote Sens. Environ. 112 (3), 1062–1080.

Straatsma, M.W., Bloecker, A.M., Lenders, H.J.R., Leuven, R.S.E.W., Kleinhans, M.G., 2017. Biodiversity recovery following delta-wide measures for flood risk reduction. Sci. Adv. 3 (11), 1–10.

Straatsma, M.W., Middelkoop, H., 2007. Extracting structural characteristics of herbaceous floodplain vegetation under leaf-off conditions using airborne laser scanner data. Int. J. Remote Sens. 28 (11), 2447–2467.

Tucker, C.J., 1979. Red and photographic infrared linear combinations for monitoring vegetation. Remote Sens. Environ. 8 (2), 127–150.

Verrelst, J., Geerling, G.W., Sykora, K.V., Clevers, J.G.P.W., 2009. Mapping of aggregated floodplain plant communities using image fusion of CASI and LiDAR data. Int. J. Appl. Earth Obs. Geoinf. 11 (1), 83–94.

Vierling, K.T., Vierling, L.A., Gould, W.A., Martinuzzi, S., Clawges, R.M., 2008. Lidar: shedding new light on habitat characterization and modeling. Front. Ecol. Environ. 6 (2), 90–98.

Wang, F.M., Huang, J.F., Tang, Y.L., Wang, X.Z., 2007. New vegetation index and its application in estimating leaf area index of rice. Rice Sci. 14 (3), 195–203.

Weidner, U., Förstner, W., 1995. Towards automatic building extraction from high-resolution digital elevation models. ISPRS J. Photogramm. Remote Sens. 50 (4), 38–49.

Willkomm, M., Bolten, A., Bareth, G., America, S., 2016. Non-destructive monitoring of rice by hyperspectral in-field spectrometry and UAV-based remote sensing: case study of field- grown rice in North Rhine-Westphalia, Germany. In: Int. Arch. Photogramm. Remote Sens. Spat. Inf. Sci. 1071–1077.

Zarco-Tejada, P.J., Diaz-Varela, R., Angileri, V., Loudjani, P., 2014. Tree height quantification using very high resolution imagery acquired from an unmanned aerial vehicle (UAV) and automatic 3D photo-reconstruction methods. Eur. J. Agron. 55, 89–99.